Radio-tomographic images of postmidnight equatorial plasma depletions

Matthew A. Hei,[1] Paul A. Bernhardt,[2] Carl L. Siefring,[2] Matthew R. Wilkens,[1] Joseph D. Huba,[2] Jonathan F. Krall,[2] Cesar E. Valladares,[3] Roderick A. Heelis,[4] Marc R. Hairston,[4] W. Robin Coley,[4] Jorge L. Chau,[5] and Cesar De La Jara[6]

Received 1 November 2013; accepted 7 December 2013; published 15 January 2014.

[1] For the first time, equatorial plasma depletions (EPDs) have been imaged in the longitude-altitude plane using radiotomography. High-resolution (~10 km) reconstructions of electron density were derived from total electron content (TEC) measurements provided by a receiver array in Peru. TEC data were obtained from VHF/UHF signals transmitted by the Coherent Electromagnetic Radio Tomography (CERTO) beacon on the C/NOFS satellite. EPDs generated premidnight were observed near dawn. On one night, the bubble densities were highly reduced, 100–1000 km wide, and embedded within a layerlike ionosphere. Three nights later, the EPDs exhibited similar features but were embedded in a locally uplifted ionosphere. The C/NOFS in situ instruments detected a dawn depletion where the reconstruction showed lifted EPDs, implying that the postmidnight electric fields raised sections of ionosphere to altitudes where embedded/reactivated fossil EPDs were detected as dawn depletions. Satellites flying under domelike distortions of the ionosphere may observe these distortions as broad plasma decreases (BPDs).
Citation: Hei, M. A., et al. (2014), Radio-tomographic images of postmidnight equatorial plasma depletions, *Geophys. Res. Lett.*, *41*, 13–19, doi:10.1002/2013GL056112.

1. Introduction

[2] The Communications/Navigation Outage Forecast System (C/NOFS) satellite has frequently observed postmidnight (0000–0600 local time) equatorial plasma depletions (EPDs) during the most recent solar minimum. As with early-evening EPDs [*Kelley et al.*, 2011], formation of postmidnight EPDs requires background ionospheric conditions conducive to a strong Rayleigh-Taylor Instability (RTI) [*Sultan*, 1996], which can create polarization electric fields within seed perturbations on the *F* region bottomside [*Kelley et al.*, 2011], causing the depleted plasma inside to $\mathbf{E} \times \mathbf{B}$ drift upward into the topside [*Woodman and La Hoz*, 1976; *Scannapieco and Ossakow*, 1976]. Unlike early-evening EPDs—also known variously as bubbles and depletion channels—postmidnight EPDs may be fossil depletions created in the early evening, then reactivated by postmidnight eastward electric fields originating from dynamo winds, geomagnetic activity, or other sources. A large number of unexpectedly deep/wide EPDs are seen by C/NOFS just before dawn at all satellite altitudes. Most authors divide these depletions into two classes: dawn density depletions (80–500 km zonal widths, plasma density reductions of 1–4 orders of magnitude) [*de La Beaujardière et al.*, 2009] and broad plasma decreases (BPDs; 500–2000+ km zonal widths, plasma density reductions of 1+ order of magnitude, minimal internal structuring) [*Huang et al.*, 2009]. Since some BPDs have been found to have relatively strong internal upward drifts (~100 m/s [*Huang et al.*, 2011]), while others appear to be the result of a descending ionosphere and/or have predominantly weak internal drifts (< 20 m/s [*Huang et al.*, 2009]), we find it useful to distinguish between active (former) and static (latter) BPDs.

[3] The extreme size and rapid evolution of channels have long made them difficult to study. Few observation techniques capture a significant portion of their structure. Moreover, those that do typically have severe limitations such as a limited observing geometry, low duty cycle, and/or high cost. However, computerized ionospheric tomography (CIT) [*Austen et al.*, 1988; *Bernhardt et al.*, 1998; *Pryse*, 2003; *Bust and Mitchell*, 2008] can quickly image plasma structures over a wide range of scales and a large geographic area [*Kersley et al.*, 1997], revealing all structure below an orbiting satellite. With CIT, an array of ground receivers uses the radio frequency (RF) signal from a low Earth orbit (LEO) satellite to calculate the total electron content (TEC) along satellite-receiver raypaths. The TEC measurements are used to create two-dimensional images of plasma density with horizontal/vertical resolution in the neighborhood of 10 km or better (depending on satellite orbit characteristics, ground receiver sample rate, plasma motions, etc.). This is a unique capability; no other technique provides quantitative maps of plasma density in the longitude/altitude plane with such high resolution and low operating costs. With CIT, it is possible to resolve individual depletion channels, as well as larger channel groups [*Hei et al.*, 2005]. The ~100 min orbital period typical of LEO satellites, combined with the short CIT observation time (~10 min), makes it possible to create multiple snapshots of channels as they develop throughout the night.

[4] The first radio-tomographic images of EPDs are presented here. Tomographic reconstructions were created with TEC measurements from an array of receivers in Peru. These receivers recorded the signal from the Naval Research Laboratory

[1]Sotera Defense Solutions, Herndon, Virginia, USA.
[2]Plasma Physics Division, Naval Research Laboratory, Washington, District of Columbia, USA.
[3]Institute for Scientific Research, Boston College, Chestnut Hill, Massachusetts, USA.
[4]Center for Space Sciences, University of Texas at Dallas, Richardson, Texas, USA.
[5]Leibniz Institute of Atmospheric Physics, Rostock University, Kühlungsborn, Germany.
[6]Jicamarca Radio Observatory, Instituto Geofisico del Peru, Lima, Peru.

Corresponding author: M. A. Hei, Plasma Physics Division, Naval Research Laboratory, Code 6754, 4555 Overlook Ave. SW, Washington, D. C. 20375-0001, USA. (gravitywave7@gmail.com)

0094-8276/14/10.1002/2013GL056112

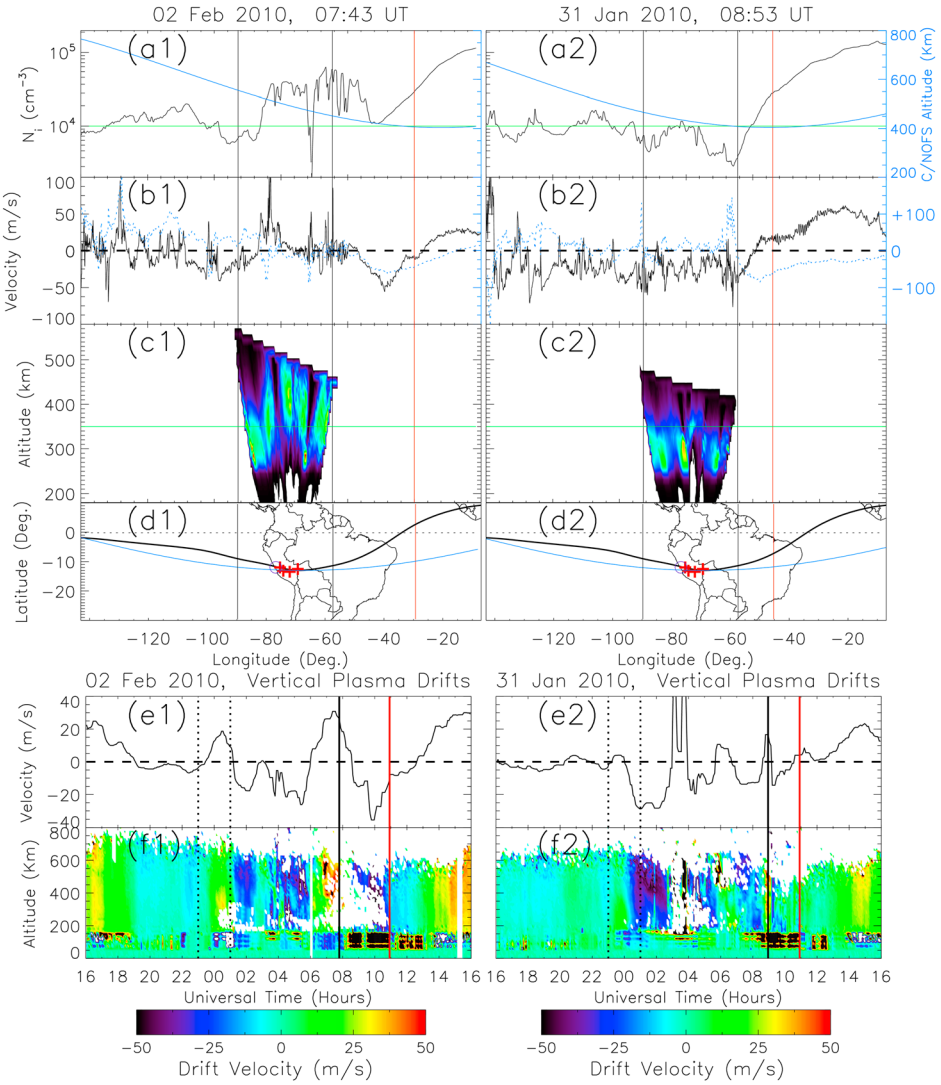

Figure 1. In situ and ground observations from 2 February and 31 January 2010. (a1, a2) CINDI in situ plasma density (black lines) and satellite altitude (blue lines). (b1, b2) In situ electric field data from the Vector Electric Field Instrument (VEFI) on C/NOFS are used to derive vertical (black lines) and zonal (dotted blue lines) plasma drift velocity. (c1, c2) NRL CERTO array tomographic reconstructions. (d1, d2) Geographic location of NWRA receivers (red crosses), JRO ISR/ionosonde (purple circle), and C/NOFS ground track (blue curves), (e1, e2) JRO ISR mean vertical plasma velocity (above 200 km), and (f1, f2) JRO ISR vertical velocity. Vertical red lines in all panels denote sunrise terminator; vertical black lines in Figures 1a1–1d1 and 1a2–1d2 denote field of view of ground receiver array; vertical black lines in Figures 1e1–1f1 and 1e2–1f2 denote ground station observation times; and dotted black lines denote nominal PRE times.

(NRL) Coherent Electromagnetic Radio Tomography (CERTO) beacon on the C/NOFS satellite [*de La Beaujardière et al.*, 2005]. The array was sited along the geomagnetic equator, yielding a longitude-altitude slice of the equatorial plasma density. In situ electron density data from the C/NOFS CINDI (Coupled Ion-Neutral Dynamics Investigation) instrument package and electron density profiles from an ionosonde stationed at Jicamarca Radio Observatory (JRO) were used to improve the quality of the reconstructions.

2. Experiment and Data Analysis

[5] The NRL CERTO receiver array consisted of four Northwest Research Associates (NWRA) ITS-33 systems sited in the Peruvian cities of Huancayo (12.04°S, 75.32°W), Ayacucho (13.16°S, 74.20°W), Cusco (13.53°S, 71.97°W), and Puerto Maldonado (12.58°S, 69.18°W). The receivers are situated very close to the geomagnetic equator, in an area of relatively low declination (Figures 1d1 and 1d2). Tomographic images created with this configuration represent longitude-altitude cross sections of EPDs extending along geomagnetic field lines in the north-south direction. For the two cases presented, the observing geometry is nearly ideal, with C/NOFS passing over the array on a west-east trajectory (Figures 1d1 and 1d2, blue curves). The imaging area was divided into an irregular grid of pixels, roughly 5 km × 5 km in the area directly over the receivers. The vertical grid spacing is constant, while the horizontal grid spacing increases from ~5 km separation above the array to ~20 km near the reconstruction edges. A Gaussian function was used to smoothly increase grid spacing when moving from the center of the image toward the sides; spacing increases slowly over the

receiver array but increases more rapidly outside this region. The resulting grid has a total number of elements on rough parity with the number of raypaths while yielding high resolution over the main image region. Additionally, this grid ensures that the horizontal image cell size exceeds the Fresnel zone length at the lowest beacon frequency (150 MHz), at least one raypath passes through each pixel, and pixels are large enough that plasma transport effects are not significant.

[6] The ground receivers provided relative TEC (RTEC) and scintillation indices by analyzing the CERTO 150/400 MHz signals with the differential phase technique [*Bernhardt and Siefring*, 2006]; RTEC was sampled at 1 Hz. The CERTO 1067 MHz signal was not used since it was turned off due to power limitations. While equatorial irregularities may cause significant scintillation in 150 MHz signals, that was not the case with the data here. The differential phase measurements are highly precise, with an accuracy of ~0.1 rad, corresponding to a TEC accuracy of 1.9×10^{13} m^{-2}. This represents a resolution of 1 part in 10^3 for a typical nighttime ionosphere. Due to the technique's inherent 2π phase ambiguity, each receiver's RTEC measurements are offset from absolute TEC (ATEC) by a constant. Receiver offsets were estimated prior to the reconstruction process, then refined within the reconstruction algorithm.

[7] Tomographic reconstructions were created using the multiplicative algebraic reconstruction technique (MART) algorithm, with ATEC estimates and an "initial guess" background ionosphere specification as initial inputs [*Na*, 1994; *Bernhardt et al*., 1998; *Kunitsyn and Tereshchenko*, 2003]. The initial guess provides information regarding the vertical structure of the ionosphere. Without such a priori information, radio tomography may not provide a unique reconstruction, since the raypaths used are mostly vertical, and thus mainly provide information regarding horizontal plasma structuring [*Kunitsyn and Tereshchenko*, 2003]. The initial guess ionosphere below the *F* peak was approximated by replicating a JRO ionosonde profile over all longitudes; above the *F* peak a Chapman function [*Hargreaves*, 1992] was fitted to the ionosonde *F* peak density and in situ CINDI measurements at each longitude. The ionosonde and fitted Chapman function densities were then interpolated onto the reconstruction grid. Receiver offsets were estimated by using the initial guess ionosphere to calculate TEC along raypaths to the satellite; the minimum TEC for a given receiver was taken as its corresponding offset.

[8] The initial guess ionosphere was also used to constrain MART to physically realistic values. Between the time of ionosonde soundings and the TEC observations, the ionosphere decays due to recombination chemistry. Moreover, below ~80 km altitude significant concentrations of plasma are unlikely. Thus, the initial guess can be used as a maximum condition to speed convergence and avoid physically unreasonable solutions. However, to allow for moderate variation of *F* peak density (N_{max}) and/or *F* peak altitude (H_{max}) with longitude during the period of observations, we take as the maximum constraint the initial guess plasma density multiplied by a constant (1.5 in this work). MART adjustments to pixel electron densities that exceed the maximum constraint are replaced with the maximum allowed densities. If the reconstruction appears to be converging to density values exceeding the maximum constraint, the multiplicative constant may be adjusted upward. Another option is to use a "two stage" reconstruction, where the first stage run is smoothed and used as the initial guess for a second run, where the multiplicative factor is increased. The second-stage initial guess is improved because the depletion locations have been identified, and the background plasma density is closer to the observations.

[9] Tomographic analysis routines were tested and optimized on a simulated bubble group created by the NRL SAMI3 code [*Huba and Joyce*, 2010]. Various one- and two-stage reconstructions were made with both MART and the algebraic reconstruction technique (ART), using different relaxation parameters, maximum constraints, iteration numbers, and simulated initial conditions. MART and ART replicated the test bubble group accurately in most cases. However, MART best resolved small-scale bottomside oscillations. Reconstructions presented here were made with single-stage MART runs with relaxation parameters [*Kunitsyn and Tereshchenko*, 2003] of 0.001.

3. Observations and Reconstructions

[10] The tomographic reconstructions (Figures 1c1 and 1c2) reveal very different ionospheric structuring. While depletion channels (blue/dark areas) exist on both nights, the background ionosphere (green/yellow) is roughly twice as thick vertically on 2 February than on 31 January. The background ionosphere was lifted to much higher altitudes (~500 km) on 2 February between 66° and 80°W longitude, leading to an apparent "arch" in the *F* layer. In contrast, almost all structure was confined below 350 km (green horizontal line) on 31 January.

[11] The uplifted section of ionosphere on 2 February manifests as a region of enhanced plasma density with embedded depletions in the CINDI data (Figure 1a1); between 57° and 83°W longitude the plasma density remains largely above 10^4 cm^{-3} (horizontal green line). A classic dawn depletion appears near 68°W longitude. The density inside the depletion is reduced by almost 2 orders of magnitude, while internal plasma drifts are ~50 m/s upward and ~50 m/s westward (Figure 1b1). Additional bubbles appear on either side of the dawn depletion; the tomographic image reveals that they just reach the satellite altitude, and are thus relatively shallow. Their internal vertical and zonal plasma drifts are generally upward and westward—again, consistent with dawn depletions. The two broad depletions flanking the uplifted region seen between 57° and 83°W in Figure 1a1 appear to be static BPDs, with zonal widths of 1500–2000 km and internal drifts somewhat downward, although the density reduction within these areas is relatively small (~1/2 order of magnitude). Note that the extended depletion region observed in the CINDI data between 82° and 90°W longitude coincides with the unraised ionosphere seen in the tomographic image. In contrast, on 31 January the CINDI plasma density remains below or just barely above 10^4 cm^{-3} (horizontal green line).

[12] Vertical plasma drifts measured by the JRO incoherent scatter radar (ISR) help explain the differences in ionospheric structuring seen on the two nights. A large upward peak (~30 m/s) in the *F* region plasma drift is centered on 0700 UT, flanked by strong downward minima (~20–40 m/s) at 0530 and 1000 UT (Figures 1e1 and 1f1). Such vertical drifts would be expected to create a wavelike modulation of the *F* peak height as observed in the tomographic images. By way of comparison, the 31 January drift data show no comparable major uplifts, and the reconstruction shows a

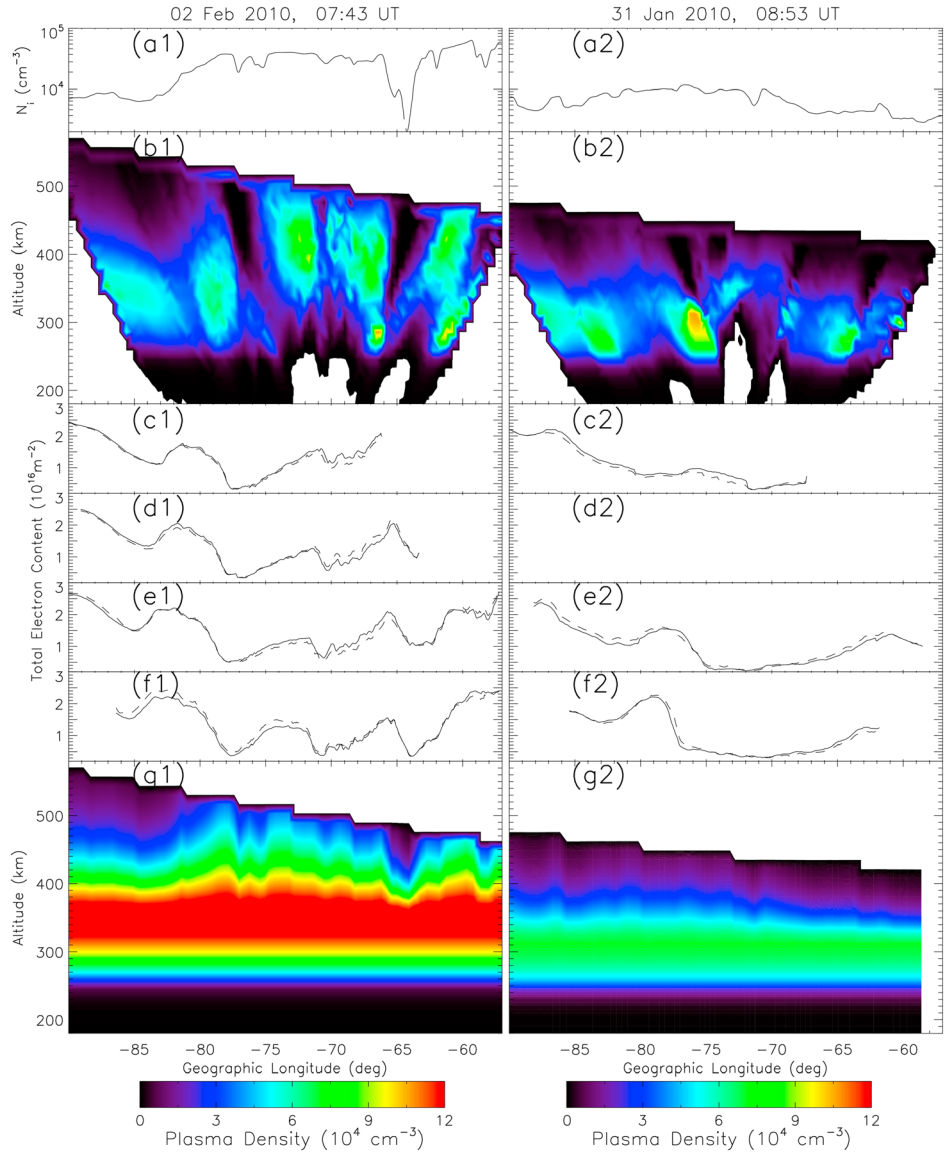

Figure 2. Elements of the tomographic reconstructions from 2 February and 31 January 2010. (b1, b2) The reconstructions are derived from (c1–f1 and c2–f2) NWRA-receiver array TEC using (g1, g2) initial guess ionospheres based on (a1, a2) CINDI in situ plasma density and ionosonde data. TEC is plotted versus the longitude of the 400 km altitude pierce point of the satellite/receiver raypath.

quiescent, layerlike ionosphere. A brief but strong uplift period does appear near 0330 UT, but this is of much shorter duration than the 2 February event.

[13] Enlarged versions of the reconstructions are shown in Figures 2b1 and 2b2. The 2 February reconstruction in Figure 2b1 reveals four depletion channels at 81°, 76°, 70°, and 64°W longitude, with widths ranging from 1° (~120 km) to roughly 4° (~480 km). The channels appear to be distributed quasiperiodically, with a spacing of ~500–700 km. The two narrowest channels (the first and third, from the left) appear to be filling in along much of their lengths, with a diffuse distribution of higher-density plasma (green on the color table) intruding on a more established low-density region. All depletion channels except the one at 81° have been lifted, along with the background ionosphere, to high (350–500 km) altitudes, suggesting the action of a localized but large-scale zonal electric field. On 31 January, three depletion channels are evident in Figure 2b2, centered on 80°, 70°, and 62°. As before, they appear to be quasiperiodically spaced, with separations of ~600–900 km; widths range from ~3° (360 km) to 8° (960 km). Depleted regions appear to be filling in, which is expected given the late observation time of the pass. Some bubble walls appear to have a slope to them, but the depletions do not have the "V" shape as seen on 2 February.

[14] The tomographic reconstructions, TEC, ISR drift velocity, in situ, and ionosonde data provide a self-consistent picture. Depletions are detected in situ by CINDI at longitudes (Figure 2a1; 65°, 71°, 76°W) where tomographic reconstructions (Figure 2b1) show uplifted bubbles; no bubbles are evident in CINDI data (Figure 2a2) when reconstructions show all irregularity structure below the satellite altitude (Figure 2b2). The lowered ionosphere between 80° and 90°W seen in Figure 2b1 also coincides exactly with the eastern half of a BPD-like depletion seen in the CINDI data. TEC (Figures 2c1–2f1 and 2c2–2g2, solid lines) shows bubbles at all longitudes where tomographic images reveal depletion

channels (subject to slight variation due to parallax); TEC and imaged depletion widths/depths are also comparable. Equatorial spread *F* (ESF)—a form of RF-interference characteristic of actively developing depletion channels—was observed in JRO ionosonde soundings during the periods when reconstructions were made (06:45–11:30 UT on 2 February and 08:15–09:15 UT on 31 January). Similar RF interference is evident in the JRO ISR vertical drift data on 2 February, when a large number of data dropouts (Figure 1f1) appear between 0700 and 1100 UT. Finally, the JRO drifts are in agreement with the large-scale ionospheric structure on both days, with the large upwelling on 2 February coinciding with a warped ionosphere and the comparatively quiescent drifts of 31 January coinciding with a layerlike ionosphere.

[15] Integration through the reconstructed electron densities yield very close agreement between the observed (Figures 2c1–2f1 and 2c2–2g2, solid lines) and calculated (dashed lines) TEC values for each receiver. The RMS difference between all observed and calculated TEC on 2 February was less than 9.49%, while on 31 January, the RMS difference was less than 7.65%. These small values indicate that the reconstructed solutions are close to the actual plasma distribution.

4. Discussion

[16] The JRO ISR data show multiple short-duration (1–3 h) uplift periods where the observed bubbles may have been spawned or reactivated. However, TEC data and preliminary tomographic images of the preceding C/NOFS orbits (not shown) reveal the existence of depletions at 0559 UT on 2 February and 0709 UT on 31 January; upward drifts after these times could lift, but not create, these bubbles. The only significant uplift on 2 February before 0559 UT is the pre-reversal enhancement (PRE) between 2300 and 0100 UT (Figure 1e1, between dashed vertical lines). This PRE is of moderate strength (~20 m/s), but observations and simulations by *Kelley et al*. [2009] show that a 16 m/s PRE is sufficient to spawn bubbles under solar minimum conditions. Thus, the 2 February bubbles likely formed around 0000 UT, then decayed until ~0600, when they were reactivated and lifted ~150 km. While ESF may appear without significant *F* region uplift [*Tsunoda et al*., 2010], the ISR drift history and ionosonde soundings reveal a low-altitude, descending ionosphere (i.e., low RTI growth rate), such that bubble formation between 0100 and 0600 UT is unlikely. On 31 January, the most probable times of bubble formation are 0000 UT (weak PRE) or 0330 UT (strong but brief uplift). *Anderson et al*. [2004] found that background upward drifts exceeding 20 m/s were highly correlated with the formation of scintillation-producing ionospheric structure. The 0330 UT drifts exceeded this forecast criterion by a factor of 2; data dropouts were also apparent in the JRO ISR data (Figure 1f2) between 0300 and 0600 UT, indicating the presence of actively developing bubbles. As on 2 February, drifts were predominantly downward outside the uplifts and therefore much less likely to spawn bubbles. Regardless of whether the 31 January bubbles formed at 0000 or 0330 UT, their origin in local time is premidnight, and postmidnight uplifts at most reactivated them.

[17] The tomographic results provide insight into the origins of the dawn density depletions and BPDs observed by C/NOFS. Previous observations [*Hysell and Burcham*, 2002] show that EPDs are common, even under solar minimum conditions. The case studies presented here reveal that postmidnight uplifts, which are common during solar minimum [*Yizengaw et al*., 2009], sometimes reactivate and lift fossil EPDs to altitudes where they are observed by C/NOFS as dawn depletions. The depletion channels imaged here had similar features, regardless of whether they were lifted to high altitudes or not. Widths ranged from ~100 to 1000 km, depletion levels were reduced from the background by ~1–2 orders of magnitude, and the bubbles were quasiperiodically spaced. These parameters are all consistent with decades of prior bubble observations [e.g., *Hei et al*., 2005; *Kelley et al*., 2011]. Two channels (the first and fourth, situated near the edges of the "arch" in the ionosphere on 2 February) appear to be "pinched off" at the bottom [*Zalesak and Ossakow*, 1980]. However, since the two central channels are not tapered in this way, it seems that dynamics associated with the local uplift of the *F* layer were the cause, rather than the faster plasma recombination chemistry characteristic of lower altitudes. The ionosphere is "tilted" in the first tomographic image, which is also a common feature of the nighttime ionosphere [*Kelley et al*., 2011].

[18] The major 2 February uplift event calls into question previous interpretations of in situ BPD observations as cross sections of wide depletion channels. Comparison of the 2 February tomographic image with the corresponding CINDI plasma density suggests that at least some BPDs are the result of C/NOFS either passing under the *F* layer or through one of the valley regions appearing on either side of an uplifted region. Specifically, comparison of Figures 1a1 and 1c1 shows that if C/NOFS had reached perigee around ~70°W instead of further to the east, it would have flown through the arched area of the ionosphere. Thus, CINDI would record an area of increased plasma density as C/NOFS pierced the western wall of the uplifted region, followed by a wide and deep depletion as it flew under the *F* layer. Plasma density enhancements are indeed commonly seen immediately to the west of BPDs, as seen in data presented by *de La Beaujardière et al*. [2009, Figures 1 and 4], *Burke et al*. [2009, Figure 1b], *Huang et al*. [2009, Figure 1], *Huang et al*. [2011, Figures 1, 2, and 3], and *Kelley et al*. [2009, Figure 3b]. In our data, the depleted region would have extended up to 11° in longitude—typical of BPDs—and would have had strong internal electric fields and drifts, consistent with an active BPD. As it happens, C/NOFS reached perigee farther to the east, observing the tops of uplifted bubbles rather than a BPD. The valley regions on either side of the uplifted region are characterized by moderate-strong downward flow, especially on the side near the dawn terminator. Thus, static BPDs may be detected when the plasma depletion in the valley region is sufficiently strong. In summary, satellite orbital characteristics may significantly influence whether dawn depletions, active BPDs, or static BPDs are observed by in situ sensors.

[19] Reports that BPDs are also very wide in latitude would appear to contradict our interpretation that (at least) some BPDs are artifacts of observing geometry—it seems unlikely that a high-inclination satellite would pass under the *F* layer over a wide swath of latitude. However, equatorial ionization anomaly (EIA) peaks persist long after sunset [*Hei and Valladares*, 2010] and may be reinforced by predawn upward drifts [*Yizengaw et al*., 2009] of magnitude comparable to the 2 February 0600–0830 event. The wide plasma density decreases seen by high-inclination satellites are therefore

likely caused by the reinforcement of remnant EIA crests by a predawn fountain effect, coupled with the satellites flying under the *F* layer near the geomagnetic equator. Indeed, International Reference Ionosphere model data presented by *de La Beaujardière et al*. [2009, Figure 5] show weak EIA crests at the time the CHAMP satellite observed a BPD 50° wide in latitude. A strong predawn fountain effect could easily reinforce the existing crests and increase their separation to the levels seen. Moreover, CHAMP's low altitude (~325 km near the depletion) maximizes the latitude range where it could fly under an uplifted *F* layer. Another wide-latitude BPD was detected by DMSP F16 and was shown to coincide with a C/NOFS-detected BPD [*Huang et al*., 2009; *Kelley et al*., 2011]. However, while the two observations are separated by only a few minutes in UT, they were widely separated in longitude. Additionally, the DMSP BPD was observed at 2030 LT, which is soon after nominal PRE time. Thus, the DMSP "BPD" is most likely not a depletion channel but rather the in situ signature of the PRE fountain effect.

[20] Possible contributors to observed postmidnight upward flows include a gravity-driven current [*Eccles*, 2004], geomagnetic activity, and a proposed dawn-sector analog to the PRE that we term the Sporadic Dawn Enhancement (SDE). In the absence of significant winds, the gravity-driven current yields significant uplift in the Peruvian sector between 0600 and 1100 UT (0100–0600 LT) [*Eccles*, 2004, Figure 1] while simultaneously suppressing the PRE. We observe strong uplifts within this period at 0700 UT on 2 February and 0630/0900 UT on 31 January, as well as moderate/small PRE drifts on both days. However, the dawn drifts exceed PRE drifts by a factor of 2 on 2 February, suggesting the action of additional uplift mechanism(s). Geomagnetic activity may provide additional uplift by inducing eastward low-latitude electric fields via penetration electric fields or the disturbance dynamo. Moderate-intensity substorms were indeed seen in the AE index on both days, with 2 February substorms reaching (350–460 nT) at 0230 and 0930 UT. Finally, we note PRE-like plasma flows at 0845 UT on 2 February and 0900 UT on 31 January. At these times—in both cases ~2 h away from the dawn terminator on the evening side—the plasma makes a rapid transition from upward to downward. As with the PRE on 2 February—which also appears ~2 h away from the (evening) terminator on the evening side—the flows are roughly symmetric in magnitude. In the case of the 2 February uplift, an "arched" ionosphere results that resembles the domelike distortion of the *F* layer often created by the PRE flows [*Kelley et al*., 2011]. We propose that eastward thermospheric winds may sporadically appear to the east of the high-pressure area associated with the midnight temperature maximum (MTM); these winds could generate eastward electric fields via the same dynamo mechanism as at the dusk terminator. Evidence for a SDE is seen in other data but often appears washed out by averaging. For example, *Huang et al*. [2012, Figure 5] showed that in October 2011 the mean *F* peak altitude reverses its postmidnight descent at ~0345 LT, rising until it reaches a local maximum at ~0500 LT, when it resumes its downward trajectory. *Fejer et al*. [1991, Figure 2] showed a local quiet-time maximum in vertical plasma drift at 0400 LT, roughly 2 h away from the dawn terminator on the nightside. Finally, *Yizengaw et al*. [2009] discovered that enhanced eastward electric fields often create a fountain effect that reinforces postmidnight EIA crests under solar minimum conditions; these electric fields appear in regions to the east of where the MTM should appear.

5. Conclusions

[21] Electron density images from satellite radio tomography have shown that strong postmidnight zonal electric fields lifted a section of ionosphere, including embedded fossil depletions, to altitudes where C/NOFS in situ sensors detected a dawn depletion and other plasma structuring. The fossil depletions originated before local midnight and were both lifted and reactivated by the electric fields. The lifting of the ionosphere by predawn electric fields is at least as important as their role in reactivating fossil depletions; without the uplift effect, bubbles may not reach high enough altitudes to be observed by in situ sensors. The domelike distortion of the *F* layer created by such postmidnight uplifts may result in the detection of BPDs by in situ sensors when a satellite flies under the *F* layer or through one of the "valley" regions on either side of the uplifted region. Thus, at least some BPDs may be artifacts of observing geometry, not actual depletion channels as has been previously assumed. The observed uplift events appear to be caused by electric fields generated by the zonal gravity current, combined with electric fields generated as the result of geomagnetic effects and/or a dawn analog of the PRE. Such a superposition would explain the predawn drifts observed on 2 February, which exceeded the earlier PRE drifts by a factor of 2.

[22] In the future, low-latitude radio beacon tomography, when combined with ionospheric models, will provide the basis to specify the ionosphere and investigate the regional development of EPDs and their effects (scintillations). Tomographic reconstructions can be used to initialize a physics-based numerical model, using depletion field-aligned symmetry to estimate plasma densities along geomagnetic field lines bisected by the tomographic imaging plane. The model can then simulate the evolution of EPDs between successive tomographic reconstructions, which are used to update the model.

[23] **Acknowledgments.** This research was supported by the NRL 6.1 Base Program, with some work completed while Matthew Hei held a National Research Council Research Associateship at NRL. The authors thank the University of Texas at Dallas for providing CINDI in situ plasma density data, the University of Massachusetts at Lowell for providing JRO ionosonde soundings, Robert Pfaff and NASA for providing the VEFI data, and the Instito Geophysico de Peru (IGP) for providing JRO ISR plasma drift data. JRO is a facility of IGP operated with support from NSF AGS-0905448 through Cornell University. The C/NOFS mission was conceived and developed by the Air Force Research Laboratory, and sponsored and executed by the USAF Space Test Program.

[24] The Editor thanks two anonymous reviewers for their assistance in evaluating this paper.

References

Anderson, D. N., B. Reinisch, C. Valladares, J. Chau, and O. Veliz (2004), Forecasting the occurrence of ionospheric scintillation activity in the equatorial ionosphere on a day-to-day basis, *J. Atmos. Sol. Terr. Phys.*, *66*, 1567–1572.

Austen, J. R., S. J. Franke, and C. H. Liu (1988), Ionospheric imaging using computerized tomography, *Radio Sci.*, *23*, 299–307.

Bernhardt, P. A., and C. L. Siefring (2006), New satellite-based systems for ionospheric tomography and scintillation region imaging, *Radio Sci.*, *41*, RS5S23, doi:10.1029/2005RS003360.

Bernhardt, P. A., et al. (1998), Two-dimensional mapping of the plasma density in the upper atmosphere with computerized ionospheric tomography (CIT), *Phys. Plas.*, *5*, 2010–2021.

Burke, W. J., O. de La Beaujardière, L. C. Gentile, D. E. Hunton, R. F. Pfaff, P. A. Roddy, Y.-J. Su, and G. R. Wilson (2009), C/NOFS observations of plasma density and electric field irregularities at post-midnight local times, *Geophys. Res. Lett.*, *36*, L00C09, doi:10.1029/2009GL038879.

Bust, G. S., and C. N. Mitchell (2008), History, current state, and future directions of ionospheric imaging, *Rev. Geophys.*, *46*, RG1003, doi:10.1029/2006RG000212.

de La Beaujardière, O., et al. (2005), C/NOFS: A mission to forecast scintillations, *J. Atmos. Sol. Terr. Phys.*, *66*, 1573-1591.

de La Beaujardière, O., et al. (2009), C/NOFS observations of deep plasma depletions at dawn, *Geophys. Res. Lett.*, *36*, L00C06, doi:10.1029/2009GL038884.

Eccles, J. V. (2004), The effect of gravity and pressure in the electrodynamics of the low-latitude ionosphere, *J. Geophys. Res.*, *109*, A05304, doi:10.1029/2003JA010023.

Fejer, B. G., E. R. dePaula, S. A. González, and R. F. Woodman (1991), Average vertical and zonal *F* region plasma drifts over Jicamarca, *J. Geophys. Res.*, *96*(A8), 13,901–13,906.

Hargreaves, J. K. (1992), *The Solar-Terrestrial Environment: An Introduction to Geospace*, Cambridge Univ. Press, Cambridge, U.K.

Hei, M. A., and C. E. Valladares (2010), The November 2004 superstorm: Comparison of low-latitude TEC observations with LLIONS model results, *J. Atmos. Sol. Terr. Phys.*, *72*, 334–343, doi:10.1016/j.jastp.2009.03.025.

Hei, M. A., R. A. Heelis, and J. P. McClure (2005), Seasonal and longitudinal variation of large-scale topside equatorial plasma depletions, *J. Geophys. Res.*, *110*, A12315, doi:10.1029/2005JA011153.

Huang, C. Y., F. A. Marcos, P. A. Roddy, M. R. Hairston, W. R. Coley, C. Roth, S. Bruinsma, and D. E. Hunton (2009), Broad plasma decreases in the equatorial ionosphere, *Geophys. Res. Lett.*, *36*, L00C04, doi:10.1029/2009GL039423.

Huang, C.-S., O. de La Beaujardiere, P. A. Roddy, D. E. Hunton, R. F. Pfaff, C. E. Valladares, and J. O. Ballenthin (2011), Evolution of equatorial ionospheric plasma bubbles and formation of broad plasma depletions measured by the C/NOFS satellite during deep solar minimum, *J. Geophys. Res.*, *116*, A03309, doi:10.1029/2010JA015982.

Huang, C.-S., O. de La Beaujardiere, P. A. Roddy, D. E. Hunton, J. O. Ballenthin, and M. R. Hairston(2012), Generation and characteristics of equatorial plasma bubbles detected by the C/NOFS satellite near the sunset terminator, *J. Geophys. Res.*, *117*, A11313, doi:10.1029/2012JA018163.

Huba, J. D., and G. Joyce (2010), Global modeling of equatorial plasma bubbles, *Geophys. Res. Lett.*, *37*, L17104, doi:10.1029/2010GL044281.

Hysell, D. L., and J. D. Burcham (2002), Long term studies of equatorial spread *F* using the JULIA radar at Jicamarca, *J. Atmos. Sol. Terr. Phys.*, *64*, 1531–1543.

Kelley, M. C., F. S. Rodrigues, J. J. Makela, R. Tsunoda, P. A. Roddy, D. E. Hunton, J. M. Retterer, O. de La Beaujardiere, E. R. de Paula, and R. R. Ilma (2009), C/NOFS and radar observations during a convective ionospheric storm event over South America, *Geophys. Res. Lett.*, *36*, L00C07, doi:10.1029/2009GL039378.

Kelley, M. C., J. J. Makela, O. de La Beaujardière, and J. Retterer (2011), Convective ionospheric storms: A review, *Rev. Geophys.*, *49*, RG2003, doi:10.1029/2010RG000340.

Kersley, L., S. E. Pryse, I. K. Walker, J. A. T. Heaton, C. N. Mitchell, M. J. Williams, and C. A. Willson (1997), Imaging of electron density troughs by tomographic techniques, *Radio Sci.*, *32*(4), 1607–1621, doi:10.1029/97RS00310.

Kunitsyn, V. E., and E. D. Tereshchenko (2003), *Ionospheric Tomography*, Springer-Verlag, Berlin.

Na, H. R. (1994), Guest Editor, Special Issue: Computerized Ionospheric Tomography, *Int. J. Imaging Syst. Technol.*, *5*, 73-187.

Pryse, S. E. (2003), Radio tomography: A new experimental technique, *Surv. Geophys.*, *24*, 1–38.

Scannapieco, A. J., and S. L. Ossakow (1976), Nonlinear equatorial spread *F*, *Geophys. Res. Lett.*, *3*, 451–454, doi:10.1029/GL003i008p00451.

Sultan, P. J. (1996), Linear theory and modeling of the Rayleigh-Taylor instability leading to the occurrence of equatorial spread *F*, *J. Geophys. Res.*, *101*, 26,875–26,891.

Tsunoda, R. T., D. M. Bubenik, S. V. Thampi, and M. Yamamoto (2010), On large-scale wave structure and equatorial spread *F* without a post-sunset rise of the *F* layer, *Geophys. Res. Lett.*, *37*, L07105, doi:10.1029/2009GL042357.

Woodman, R. F., and C. La Hoz (1976), Radar observations of *F* region equatorial irregularities, *J. Geophys. Res.*, *81*(31), 5447–5466, doi:10.1029/JA081i031p05447.

Yizengaw, E., M. B. Moldwin, Y. Sahai, and R. de Jesus (2009), Strong postmidnight equatorial ionospheric anomaly observations during magnetically quiet periods, *J. Geophys. Res.*, *114*, A12308, doi:10.1029/2009JA014603.

Zalesak, S. T., and S. L. Ossakow (1980), Nonlinear equatorial spread *F*: Spatially large bubbles resulting from large horizontal scale initial perturbations, *J. Geophys. Res.*, *85*, 2131–2142.